Numerical Study of the Daytime Planetary Boundary Layer over an Idealized Urban Area: Influence of Surface Properties, Anthropogenic Heat Flux, and Geostrophic Wind Intensity

SERENA FALASCA*

Department of Physical and Chemical Sciences, University of L'Aquila, L'Aquila, Italy

FRANCO CATALANO

ENEA, Rome, Italy

MONICA MORONI

Department of Civil, Constructional and Environmental Engineering, Sapienza University of Rome, Rome, Italy

(Manuscript received 19 May 2015, in final form 26 September 2015)

ABSTRACT

Large-eddy simulations of an idealized diurnal urban heat island are performed using the Weather Research and Forecasting Model. The surface energy balance over an inhomogeneous terrain is solved considering the anthropogenic heat contribution and the differences of thermal and mechanical properties between urban and rural surfaces. Several cases are simulated together with a reference case, considering different values of the control parameters: albedo, thermal inertia, roughness length, anthropogenic heat emission, and geostrophic wind intensity. Spatial distributions of second-moment statistics, including the turbulent kinetic energy (TKE) budget, are analyzed to characterize the structure of the planetary boundary layer (PBL). The effect of each control parameter value on the turbulent properties of the PBL is investigated with respect to the reference case. For all of the analyzed cases, the primary source of TKE is the buoyancy in the lower half of the PBL, the shear in the upper half, and the turbulent transport term at the top. The vertical advection of TKE is significant in the upper half of the PBL. The control parameters significantly influence the shape of the profiles of the transport and shear terms in the TKE budget. Bulk properties of the PBL via proper scaling are compared with literature data. A log-linear relationship between the aspect ratio of the heat island and the Froude number is confirmed. For the first time, the effect of relevant surface control parameters and the geostrophic wind intensity on the bulk and turbulent properties of the PBL is systematically investigated at high resolution.

1. Introduction

At present, around half the world's population lives in cities, and the percentage is projected to reach 67% by 2050. As the heart of human activities, urban areas account for 60%–80% of global energy consumption and around the same share of anthropogenic CO_2 emissions (European Environment Agency 2014). Such a rapid increase of the urbanization phenomenon will significantly impact the quality of urban life and lead to modifications of the urban climate.

The urban climate mainly depends on the surface energy balance (SEB), which is influenced by alterations to the land characteristics due to human activities; the result of such direct and indirect modifications is urban warming (Hinkel et al. 2003), or urban heat island (UHI), and the associated circulation (Catalano et al. 2012a; Ryu et al. 2013). There are cases where the latent heat flux in urban areas is higher than in rural areas (e.g.,

* Additional affiliation: Department of Civil, Constructional and Environmental Engineering, Sapienza University of Rome, Rome, Italy.

Corresponding author address: S. Falasca, Department of Physics, University of L'Aquila, via Vetoio, 67010 Coppito, L'Aquila, Italy.
E-mail: serena.falasca1@univaq.it

DOI: 10.1175/JAMC-D-15-0135.1

the city of Phoenix, built in a desert area), and thus the temperature in the rural area is higher than in the urban area; the occurrence of this phenomenon, called ''urban cool island,'' is evidenced in the literature (Lee and Baik 2010; Giovannini et al. 2011). Though the UHI is typically a nocturnal phenomenon, field measurements have proven that the daytime temperature in the city can be higher than in the surrounding rural area (Kim and Baik 2002; Hidalgo et al. 2008). Furthermore, the UHI phenomenon may synergistically interact with heat waves, increasing heat stress in urban areas (Li and Bou Zeid 2013). The need for a healthier urban environment is widely recognized, as is the influence of each SEB parameter on urban meteorology. Grimmond and Oke (1999) showed that the time evolution of each component of the SEB equation is a particular characteristic of the site; furthermore, the contribution of each term in the surface energy equation varies as a function of the site properties and influences the structure of the UHI plume.

Several studies have investigated the UHI effects on human health (Milojevic et al. 2011), energy and water consumption (Akbari et al. 2001), precipitation (Miao et al. 2011), and global warming (Chen et al. 2006). Martilli (2002) studied the effect of wind speed, urban morphology, and rural soil moisture on the structure of the nocturnal and diurnal planetary boundary layer in the presence of an urban area using a 2D mesoscale model, considering also the effects of the UHI flow on the dispersion of a passive tracer. Catalano et al. (2012a) analyzed the effects of some relevant parameters (i.e., UHI characteristic dimension, Brunt–Väisälä frequency, thermal forcing nature) on velocity and temperature variances at the UHI center. Wang (2009) reproduced the circulation associated with the urban–rural differential surface sensible heat flux and roughness to investigate the influence of the circulation on the convective boundary layer (CBL). Even though a large-eddy simulation (LES) model (Bryan and Fritsch 2002) is employed as well as the same domain configuration as the present study, Wang (2009) does not take into account the influence of the geostrophic wind and land properties on the UHI circulation and on the structure of the CBL; this subject is the focus of the present study. The analysis of the turbulent structure of the PBL provides important parameters for the investigation of pollutant dispersion dynamics (Roth 2000). Most of the numerical studies of the urban flows with the Weather Research and Forecasting (WRF) Model are based on meteorological mesoscale simulations coupled with suitable parameterization schemes (Salamanca et al. 2011; Giovannini et al. 2014). The LES technique has been recently applied to high-spatial-resolution simulations of heterogeneous terrains (Catalano and Cenedese 2010; Catalano and Moeng 2010) with idealized bottom boundary conditions (Catalano et al. 2012a).

Salamanca et al. (2011) and Giovannini et al. (2014) investigated the boundary layer characteristics in the presence of an urban site with the WRF Model, with a resolution of 500 m, using urban parameterization schemes. The WRF Model has also been used by Li et al. (2013) to analyze land–atmosphere interactions and the PBL structure for an urban environment in a case of heavy rainfall with a resolution on the order of 1 or more kilometers.

Ryu et al. (2013) investigated the structure and evolution of an idealized daytime UHI through numerical simulations with the WRF Model; their work focused on the interaction of the UHI with the convective cells over urban and rural areas, but turbulent properties of the flow pattern were not considered. The vertical structure of the planetary boundary layer (PBL) associated with the UHI circulation was also investigated by Filho et al. (2013) by means of a LES model; the PBL height was computed following the classical method based on the maximum value of the vertical potential temperature gradient. In their work the turbulent structure of the PBL associated with the UHI circulation is not investigated.

The objective of this paper is the investigation of the influence of parameters appearing in the SEB terms (albedo, thermal inertia, and anthropogenic heat flux) and mechanical parameters (geostrophic wind intensity, roughness length) on the structure of the PBL over urban areas during the daytime. To assess the sensitivity to specific control parameters, ad hoc idealized simulations are more effective than real test cases in which it is more difficult to separate the effects of each parameter on the phenomenon. LESs of the diurnal UHI have been performed using the WRF Model (Skamarock et al. 2008). The surface heat flux (SHF) has been calculated from the net incident radiation and accounts for different land properties of urban and rural areas. We investigated 11 cases, considering different values of the control parameters. Distributions of second-order statistics and the turbulent kinetic energy (TKE) budget are analyzed to characterize the turbulence associated with the UHI flow.

The paper is organized as follows. In section 2, a description of the methodology, including the numerical setup and the scaling approach, is presented. Results are presented in section 3, and conclusions are given in section 4.

2. Method

a. *Numerical setup*

The simulations have been performed with the WRF Model in large-eddy simulation mode. The WRF Model

is a nonhydrostatic model based on fully compressible Euler equations (Skamarock et al. 2008). The spatial discretization for the variables is based on a staggered Arakawa C–type grid. Given the limited horizontal scales of the UHI phenomenon, Coriolis terms in the momentum equation are neglected in the present investigation.

The domain has $400 \times 100 \times 58$ grid nodes along the x, y, and z directions, respectively. The grid has a horizontal constant resolution equal to 50 m and a vertical parabolic stretching such that Δz grows from 2 m above the ground to 90 m at the top of the domain. The vertical coordinate is terrain-following normalized pressure.

The urban area considered in the model has dimensions of 2000 m $\times$ 5000 m and is centered with respect to the x axis. Periodic lateral boundary conditions are imposed on both x and y directions to mimic an infinite succession of UHI along the x direction and an infinitely long urban site along the y direction. At the model top, constant pressure, free slip, and zero vertical velocity conditions are assumed. The atmosphere and the soil are assumed to be dry.

The surface model is based on the Monin–Obukhov similarity theory (Monin and Obukhov 1954), and the 5-layer slab land surface scheme is used (Skamarock et al. 2008).

The time integration consists of a third-order Runge–Kutta scheme with a smaller time step for acoustic modes. The spatial discretization uses fifth- and third-order advection schemes for the horizontal and the vertical integration, respectively.

The subgrid-scale (SGS) model is a modified version of the WRF TKE scheme, which accounts for the effect of the grid's anisotropy in the calculation of the filter width (Catalano and Moeng 2010; Catalano and Cenedese 2010); a detailed description of the SGS terms and expressions is provided in Catalano and Cenedese (2010).

The UHI is simulated using the radiative forcing based on the SEB equation (Deardorff 1978). Urban canopy models are not used since they are developed for mesoscale applications and they are not suitable for LES simulations (Kusaka and Kimura 2004). Urban geometries (e.g., the immersed boundary layer method) are also not used.

The WRF Model has been modified to explicitly take into account the bulk urban features. Different values of albedo, thermal inertia, and roughness length are imposed at the urban and rural areas. Radiative schemes have been modified to work in LES mode and have been adapted to idealized simulations (e.g., dry atmosphere). Furthermore, the SEB equation has been modified to take into account the production of anthropogenic heat over the urban area and to remove the latent heat flux term. Thus,

$$(1-\alpha)R_S\downarrow + R_L^* + Q_f - H_{\rm sg} = Q_G, \qquad (1)$$

where α is the albedo, $R_S\downarrow$ is the incident shortwave (SW) radiation, R_L^* is the net longwave (LW) radiation at the surface, Q_f is the anthropogenic heat, $H_{\rm sg}$ is the sensible heat flux at the ground toward the atmosphere, and Q_G is the soil heat flux. The SW radiation term $(1-\alpha)R_S\downarrow$ is computed using the Dudhia scheme (Dudhia 1989) and the same value of the incident radiation $R_S\downarrow$ is imposed over the entire domain. The net LW radiation R_L^* is assumed to be constant according to the parameterization proposed by Burridge and Gadd (1975). Different reflective, mechanical, and thermal properties of the surface are set to reproduce the different thermal behavior of the urban and rural areas. The net radiative forcing is modeled by a sinusoidal law. The simulations start with an incident SW equal to zero and a stably stratified environment, characterized by a Brunt–Väisälä frequency N of 0.0128 $\rm s^{-1}$. This condition roughly corresponds to the end of nighttime. LES studies in literature (Kurbatskii 2001; Catalano et al. 2012a) expressed the thermal forcing at the bottom boundary of the domain in terms of either SHF or the surface temperature anomaly. In the first case, the SHF corresponding to the urban area was directly imposed in the energy equation, while in the second case the surface temperature was imposed. In the present study, the incident radiation is imposed and the surface energy equation is solved taking into account the local properties of the surface. This allows a better representation of land–atmosphere feedbacks.

Control parameters for the simulations are (i) geostrophic wind intensity, (ii) surface roughness, (iii) albedo, (iv) thermal inertia, and (v) anthropogenic heat emission. Among them, albedo, thermal inertia, and anthropogenic heat appear in the SEB equation; albedo influences the net radiation at the surface and therefore the SHF, while thermal inertia influences the response of the soil to the radiation in terms of surface temperature. The surface roughness influences the wind field on both the urban and rural areas through the shear production term on the momentum equation.

We conducted 11 numerical simulations of the diurnal UHI. The domain and urban area dimensions are the same for all the cases as well as the initial ambient temperature profile and the incident solar radiation. The incident SW radiation is set equal to 450 $\rm W\,m^{-2}$ and the net LW radiation is set equal to -50 $\rm W\,m^{-2}$. The control parameter values are reported in Table 1.

Case 1 is the reference case; the other simulations investigate the influence of each control parameter; therefore, each simulation presents the same values of the parameters as case 1, except for one. In cases 2–4 an

TABLE 1. Numerical simulations, values of control parameters, and computed parameters at $t = 1200$ LST (the anthropogenic heat flux has a sinusoidal time evolution with a period of 24 h). The U and R stand for urban and rural, respectively.

Case	v_g ($m\,s^{-1}$)	Roughness z_0 (m) U	Roughness z_0 (m) R	Albedo difference $\Delta_{R\text{-}U}$	Thermal inertia ($J\,m^{-1}\,K^{-1}\,s^{-0.5}$) U	Thermal inertia ($J\,m^{-1}\,K^{-1}\,s^{-0.5}$) R	Anthropogenic heat ($W\,m^{-2}$)	$\overline{w'\theta'_s}$ ($K\,m\,s^{-1}$) U	$\overline{w'\theta'_s}$ ($K\,m\,s^{-1}$) R	$\Delta\theta_m$ (K)	z_i (m)
1	0	0.1		0.30	20.9	12.6	0	0.170	0.105	2.42	1106
2	2	0.1		0.30	20.9	12.6	0	0.175	0.105	2.18	1107
3	5	0.1		0.30	20.9	12.6	0	0.171	0.106	2.55	1107
4	10	0.1		0.30	20.9	12.6	0	0.177	0.109	2.65	1107
5	0	0.3	0.1	0.30	20.9	12.6	0	0.178	0.105	1.63	1106
6	0	0.5	0.1	0.30	20.9	12.6	0	0.179	0.105	1.24	1106
7	0	0.1		0.45	20.9	12.6	0	0.179	0.063	4.15	994
8	0	0.1		0.65	20.9	12.6	0	0.196	0.011	7.23	697
9	0	0.1		0.30	8.34	12.6	0	0.222	0.104	3.89	1165
10	0	0.1		0.30	20.9	12.6	25 ± 25/2	0.197	0.106	3.19	1165
11	0	0.1		0.30	20.9	12.6	40 ± 40/2	0.211	0.105	3.61	1165

along-y geostrophic wind has been imposed, with intensity of 2, 5, and $10\,m\,s^{-1}$, respectively. Cases 5 and 6 have different values of the roughness z_0 of the urban area with respect to the rural area. In cases 7 and 8 different values of albedo difference between rural and urban areas have been considered. Thermal inertia is the control parameter for case 9. In cases 10 and 11 an anthropogenic heat flux with a sinusoidal time evolution has been imposed with a mean value of $25\,W\,m^{-2}$ for case 10 and of $40\,W\,m^{-2}$ for case 11, and with an amplitude equal to half the mean value in both cases (Table 1).

b. Averaging procedure and parameters calculation

In this study, the only homogeneous direction is along the y axis because of the geometry of the urban site (infinite along the y direction and finite along the x direction). Therefore, first- and second-moment statistics are obtained by averaging along the y axis. The average value of the considered variable ϕ is

$$\overline{\phi} = \frac{1}{N_y}\sum_{j=1}^{N_y}\phi_j, \tag{2}$$

where N_y is the number of cells in the y direction. The perturbations ϕ' are defined as follows:

$$\phi'(x,y,z,t) = \phi(x,y,z,t) - \overline{\phi}(x,z,t). \tag{3}$$

Furthermore, to increase robustness, statistics are further averaged along five contiguous grid cells in the x direction (Catalano and Moeng 2010).

Because of the inhomogeneous surface properties, the PBL height z_{PBL} must be locally defined. Hence, the PBL height is computed according to the hybrid method proposed by Catalano and Moeng (2010) for an inhomogeneous terrain; z_{PBL} is defined as the lowest height where two constraints are verified: the magnitude of the potential temperature vertical gradient is larger than a critical value (expressed as 80% of its maximum value) and the heat flux is less than 15% of its maximum value. In Catalano et al. (2011) the hybrid method is compared with the classical methods (Sullivan et al. 1998) showing more accurate estimates of z_{PBL} overall the domain and comparable results in correspondence with the UHI center.

The UHI intensity is a bulk parameter characterizing the UHI phenomenon; it is defined as the temperature difference between urban and rural areas and is computed at $x/D = 0$ as the difference in the mixing layer between urban and rural temperature averaged along the y direction.

c. Scaling

Results are normalized following the similarity theory proposed by Lu et al. (1997a,b), according to which the UHI circulation is characterized by three parameters: the characteristic dimension of the urban area D, the Brunt–Väisälä frequency N of the undisturbed atmosphere, and the SHF H_0. The scale quantities are the mixing height of the UHI z_i, the horizontal velocity scale $w_D = (g\beta H_0 D)^{1/3}$, and the vertical velocity scale $w_L = w_D^2/ND$. The time scale is defined as $t_L = D/w_D$. For temperature, two scales are defined: the mean temperature scale given by the UHI intensity, generically indicated with $\Delta\theta_m$, and the convective temperature scale $\theta_L = w_D N/g\beta$. The latter is employed to normalize the turbulent fluxes. Turbulent statistics are normalized according to the similarity theory by Lu et al. (1997a,b): velocity variances are normalized by w_D^2, the heat flux by H_0, and the TKE by w_D^3/z_i. The z axis is normalized with the mixing height z_i and the x axis is normalized with the characteristic dimension D.

Scale quantities and parameters are combined to form two nondimensional numbers: the Reynolds number

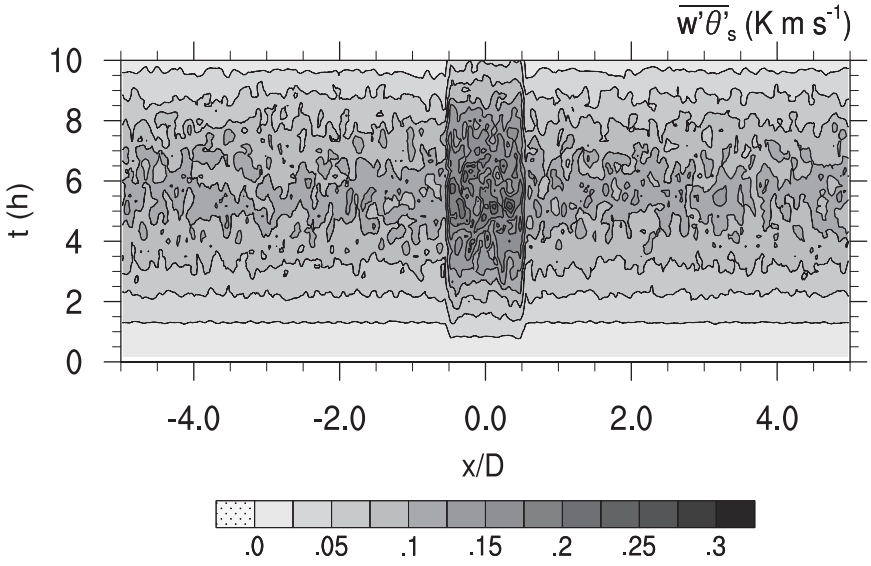

FIG. 1. Hovmöller plot of the y-averaged surface kinematic heat flux for case 1 (reference case). The horizontal axis is normalized by the horizontal dimension of the urban area D.

$\mathrm{Re} = w_D D/\nu$, where ν is the fluid kinematic viscosity, and the Froude number $\mathrm{Fr} = w_D/ND$. If the Re value is above a critical value corresponding to a fully turbulent flow, Fr is the only nondimensional number required to describe the phenomenon (Snyder 1981; Lu et al. 1997a).

This theory has been developed for low aspect ratio ($z_i/D \ll 1$) nocturnal UHIs. Cenedese and Monti (2003) and Catalano et al. (2012a) have shown that the similarity theory proposed by Lu et al. (1997a,b) can be applied also to daytime UHIs. Falasca et al. (2013) have applied the theory of Lu et al. (1997a,b), obtaining a detailed flow characterization of the UHI circulation by means of high-resolution data measured during experimental acquisitions. Other scaling laws have been proposed by Hidalgo et al. (2010) for the diurnal UHI; Catalano et al. (2012b) proposed an alternative scaling for the free convection, potentially applicable to the UHI.

3. Results

a. UHI bulk properties

The difference of the SHF between rural and urban areas plays a major role in the development of the UHI circulation. The time–space evolution of the y-averaged SHF for case 1 is shown as Hovmöller plot in Fig. 1. Larger values of the SHF characterize the urban area during the central hours of the simulation, that is, between 1000 local standard time (LST) and 1400 LST. The SHF step corresponds approximately to the urban area boundaries. The spatial inhomogeneity of the SHF affects the PBL height; this can be seen in Fig. 2 where z_{PBL} is plotted as a function of the distance from the urban area center at different simulation times for the reference case. The step in the SHF plot has a counterpart in the z_{PBL} plot, mainly evident at 0700 LST. For longer simulation times the SHF is more uniform along the x direction as well as the z_{PBL}.

Figure 2 further compares the PBL height as a function of the distance from the urban area center at different simulation times of the reference case with cases 7 and 11. To improve the visualization, the vertical axis is extended up to 1200 m, while the simulated domain is 2400 m high. At $t = 1$ h, the presence of the UHI determines a step in the evolution of the PBL height at the center of the domain. The effect of the urban area on z_{PBL} is felt up to $x/D = \pm 0.5$ for cases 1 and 7, and it is felt up to $x/D = \pm 1$ for case 11. At $t = 3$ h and $t = 6$ h the difference of z_{PBL} between urban and rural areas is drastically reduced because of the development of convective cells over the rural area levels. Table 1 shows the bottom forcing intensity at $t = 1200$ LST for all the cases, the UHI intensity $\Delta\theta_m$, and the PBL height at the UHI center z_i. The UHI intensity is directly influenced by albedo, thermal inertia, and anthropogenic heat, which appear in the SEB equation (increasing urban–rural albedo gap, anthropogenic heat flux, and urban thermal inertia correspond to increasing $\Delta\theta_m$), and is indirectly influenced by geostrophic wind and roughness. The geostrophic wind intensity (up to 10 m s^{-1}) has light influence on the UHI intensity. The larger roughness length over the urban area in case 6 dampens the

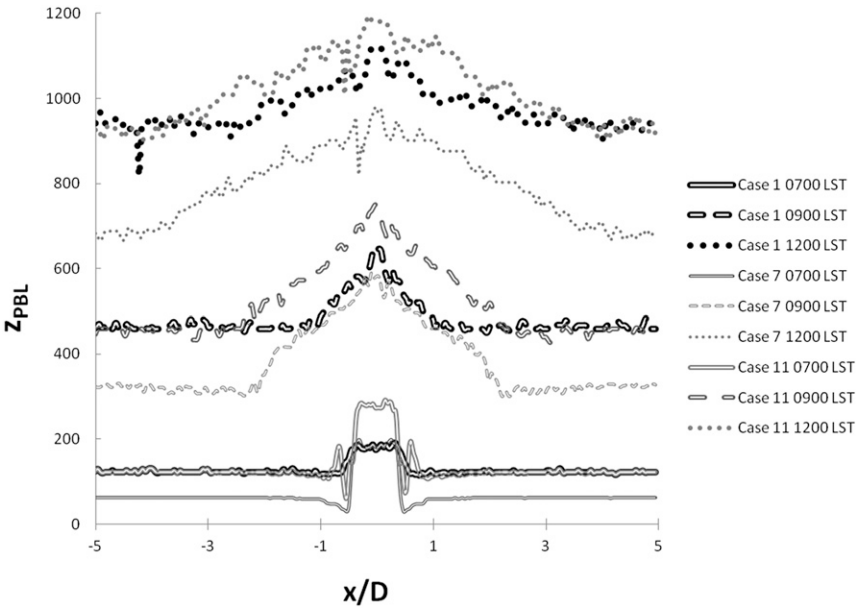

FIG. 2. Plot of the PBL height as a function of the distance from the UHI center for different simulation times for cases 1, 7, and 11.

mixed-layer development there and weakens the convergence at the surface. Since the surface breeze has the effect of inhibiting thermals growth over the rural area, a weaker current with respect to the reference case facilitates the development of the mixed layer over the rural area in case 6. This mechanism results in a reduction of mixed-layer temperature differences between the urban and the rural areas, then a reduction of the UHI intensity.

The height z_i is affected by thermal surface properties and by anthropogenic heat. Cases 7 and 8 (control parameter albedo) have smaller values of z_i. Cases 10 and 11 (control parameter anthropogenic heat flux) present larger values of z_i.

Figure 3 shows the UHI aspect ratio (z_i/D) versus Fr for results obtained in the present study only for diurnal UHIs, compared with literature data for both diurnal and nocturnal UHIs. Catalano et al. (2012a) use the WRF Model and the same domain configuration as in this work to investigate the effect of the diameter and the Brunt–Väisälä frequency on the UHI bulk parameters. Hidalgo et al. (2010) used the Meso-NH to simulate a diurnal (circular) UHI with no mean wind. Kristof et al. (2009) performed simulations by means of the ANSYS, Inc., Fluent 6 solver. Kurbatskii (2001) employed a three-equation model for turbulent transport over a circular urban area in a stably stratified environment. Richiardone and Brusasca (1989) modeled a diurnal UHI under calm conditions. Wang (2009) performed daytime LES of an infinite urban area with no geostrophic wind using the model by Bryan and Fritsch (2002). Yoshikado (1992) used a two-dimensional model to simulate a diurnal UHI with no background wind. Figure 3 also includes laboratory experiments conducted in different water tank facilities by Cenedese and Monti (2003) (urban area with circular shape), by Falasca et al. (2013) (rectangular shape), and by Lu et al. (1997a,b) (circular shape). Experimental contributions by Faust (1981), field observations by Clarke and McElroy (1974), and Godowitch et al. (1987) have been included as well.

All data fall on a log-linear relationship of equation $\ln(z_i/D) = 2.92\ \ln(\mathrm{Fr})$ between the PBL height at the UHI center z_i and the Fr number. Lu et al. (1997a) showed a plot of z_i/D versus Fr using experimental and field results, and the resulting best-fit line was $\ln(z_i/D) = 2.86 \ln(\mathrm{Fr})$; Catalano et al. (2012a) presented a similar plot using also numerical results, and the resulting regression-line slope was 2.91. We added other numerical results, obtaining a slope of 2.92. Such a relationship between Fr and the UHI aspect ratio links z_i to the SHF, to the Brunt–Väisälä frequency, and to the urban area characteristic dimension. Field data are characterized by lower values of the aspect ratio and Fr; on the other side, laboratory experimental results have higher values of Fr and aspect ratio; numerical results occupy the central area of the picture, characterized by a wide range of intermediate values of z_i/D and Fr.

b. *Second-moment statistics*

Figure 4 shows the y-averaged second-moment statistics (TKE, horizontal and vertical velocity variances,

and fluxes, respectively) and the PBL height estimate for case 1 at $t = 1200$ LST. The largest values of TKE are located over the urban area between $0.3 < z/z_i < 0.8$, where TKE reaches values about 4 times larger than those at the boundary of the domain, and the turbulence intensity decreases with increasing distance from the urban area; the influence of the UHI is evident up to a distance from the urban area center equal to twice D.

The w variance gives the most important contribution to the TKE over the urban area (Fig. 4d). The horizontal variances present higher values over the urban area than over the rural one. The large contribution from the w variance to turbulence both over the urban area and outside is consistent with the main structure of the CBL (Moeng and Sullivan 1994; Catalano et al. 2012b).

The vertical heat flux is positive except over the urban area near the PBL top (Fig. 4f); the small area with negative buoyancy flux at the top of the PBL, in correspondence with the urban area center, is the entrainment area.

The vertical cross sections of the y-averaged TKE and the vertical profiles of variances and fluxes at $t = 1200$ LST are shown in Figs. 5–10 for a selection of simulations. Cases 4, 6, 7, 9, and 11 are chosen since they are the most representative of the effects of the control parameters on flow structure and distribution of the second-moment statistics.

Horizontal variances display vertical profiles similar to those of a free convection PBL (Moeng and Sullivan 1994), except for the relative maximum at intermediate altitude (Figs. 6a, 7a, 8a, and 9a). The velocity vertical component variance has a parabolic shape that recalls that of the free convection PBL, except for the decrease at about $0.6z_i$ and the step near the PBL top. (Figure 10 shows that the normalized heat flux decreases from $z/z_i = 0.2$ reaching the minimum value of -0.5 in correspondence with the PBL height.)

The velocity flux $\overline{u'w'}$ is positive in the lower part (up to $0.4z_i$), where the flux is convergent, and at the top of the PBL (Fig. 9). The presence of a small positive value of $\overline{u'w'}$ at $z/z_i = 1.2$ may be related to the presence of gravity waves.

The presence of the geostrophic wind of $v_g = 10\,\mathrm{m\,s^{-1}}$ influences the values of TKE and the structure of the turbulent boundary layer: in case 1 (with no geostrophic wind), the TKE intensity decreases from the urban area center (where larger values are located) and a significant influence of the UHI is evident in the domain region where $-2 < x/D < 2$ (Fig. 4a), while in case 4 (with $v_g = 10\,\mathrm{m\,s^{-1}}$) there is evidence of the influence of the UHI in a smaller area around the UHI center (Fig. 5a). In correspondence with the urban area center, values of TKE are between 1 and $4\,\mathrm{m^2\,s^{-2}}$ for case 4 with the maximum located near the surface, while in case 1 they are between 0.5 and $2\,\mathrm{m^2\,s^{-2}}$. Over the rural area, TKE values are between 0.5 and $1\,\mathrm{m^2\,s^{-2}}$ in both cases 1 and 4. The presence of the geostrophic wind of increasing intensity determines modifications of the u-variance vertical profile (Fig. 6b); such modifications make this profile similar to the typical profile of a shear-driven PBL with the maximum near the surface (Moeng and Sullivan 1994). The lower maximum of the u variance for case 4 is near the surface and is about 7 times larger than the lower maximum for case 1 because of the important contribution of the horizontal shear in this simulation; the upper maximum for case 4 is located at the PBL top and is about 2 times larger than the maximum in case 1. The v variance shows the presence of the maximum in correspondence with the inversion height typical of the shear-driven PBL (Fig. 7b); at the top of the domain, the v variance gives an important contribution to turbulence, with a maximum of about 4 times the upper maximum for case 1. The parabolic profile of the w variance in case 1 is less evident in case 4

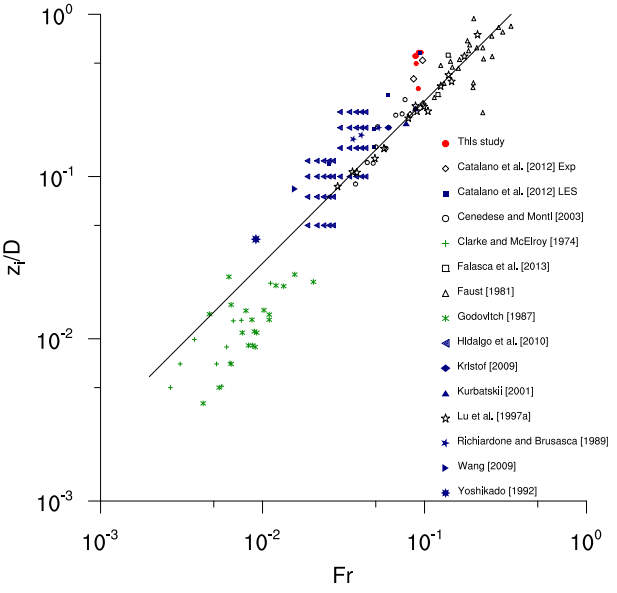

FIG. 3. Ratio of UHI aspect ratio z_i/D vs Fr for numerical results of the present paper compared with literature data. Numerical results of Hidalgo et al. (2010), Kristof et al. (2009), Kurbatskii (2001), Richiardone and Brusasca (1989), Wang (2009), and Yoshikado (1992); laboratory experiments of Cenedese and Monti (2003), Falasca et al. (2013), Faust (1981), and Lu et al. (1997a); field observations of Clarke and McElroy (1974) and Godowitch et al. (1987). Both axes have a logarithmic scale. The regression (solid) line has a slope of 2.92.

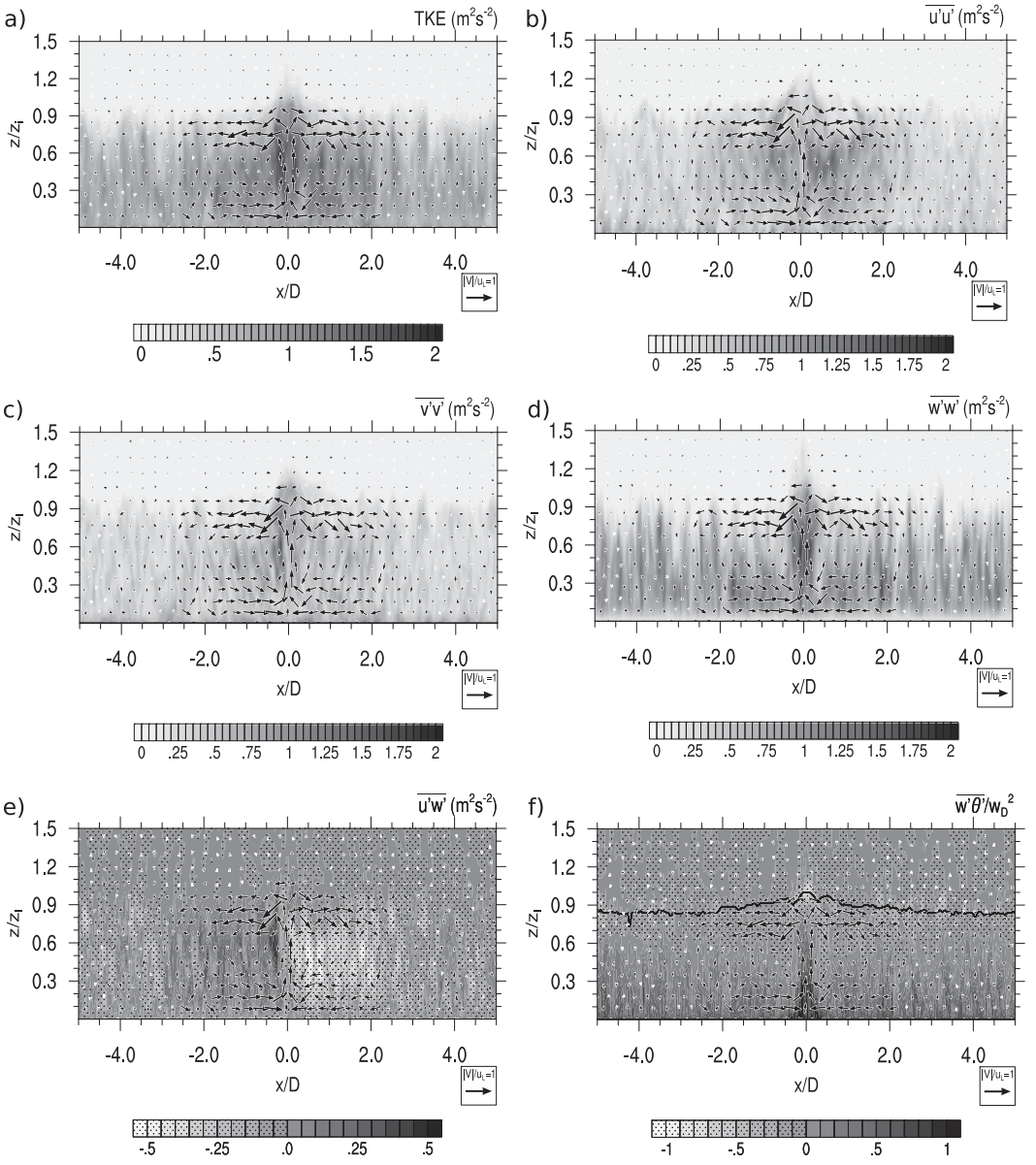

FIG. 4. Vertical cross sections of the y-averaged second-moment statistics along with wind vectors: (a) TKE, (b) $\overline{u'u'}$, (c) $\overline{v'v'}$, (d) $\overline{w'w'}$, (e) $\overline{u'w'}$, and (f) $\overline{w'\theta'}$ at $t = 6$ h for case 1 (reference case). The y axis is normalized by the inversion height z_i. The black line in (a) represents the normalized PBL depth estimate.

where it presents two maxima, one located at $z = 0.5z_i$, slightly larger than that of case 1, and one at $z = 1.2z_i$ (Figs. 8a,b).

Figure 5b shows the effects of the difference of roughness length values between urban and rural areas on the TKE; a z_0 positive difference of 0.4 determines an increase of the TKE over the urban area in case 6; the maximum location is the same (about $z/z_i = 0.5$), but the value is less evident in case 6. A slight increase of the values on the rural area is evident. Similarly to case 4, the u-variance profile of case 6 (Fig. 6c) presents a maximum near the surface, equal to twice the lower maximum in case 1. Values in the upper part of the layer, between $z/z_i = 0.4$ and 0.8, are larger than in case 1. The v variance shows a general increase of the values, especially near the surface (Fig. 7c). The w variance presents two maxima, at $0.2z_i$ and $0.8z_i$ (Fig. 8c).

The effect of a change in the urban–rural albedo contrast (from 0.45 in case 1 to 0.6 in case 7) is evident in the reduction of the mixing height over the rural area due to the higher value of rural albedo,

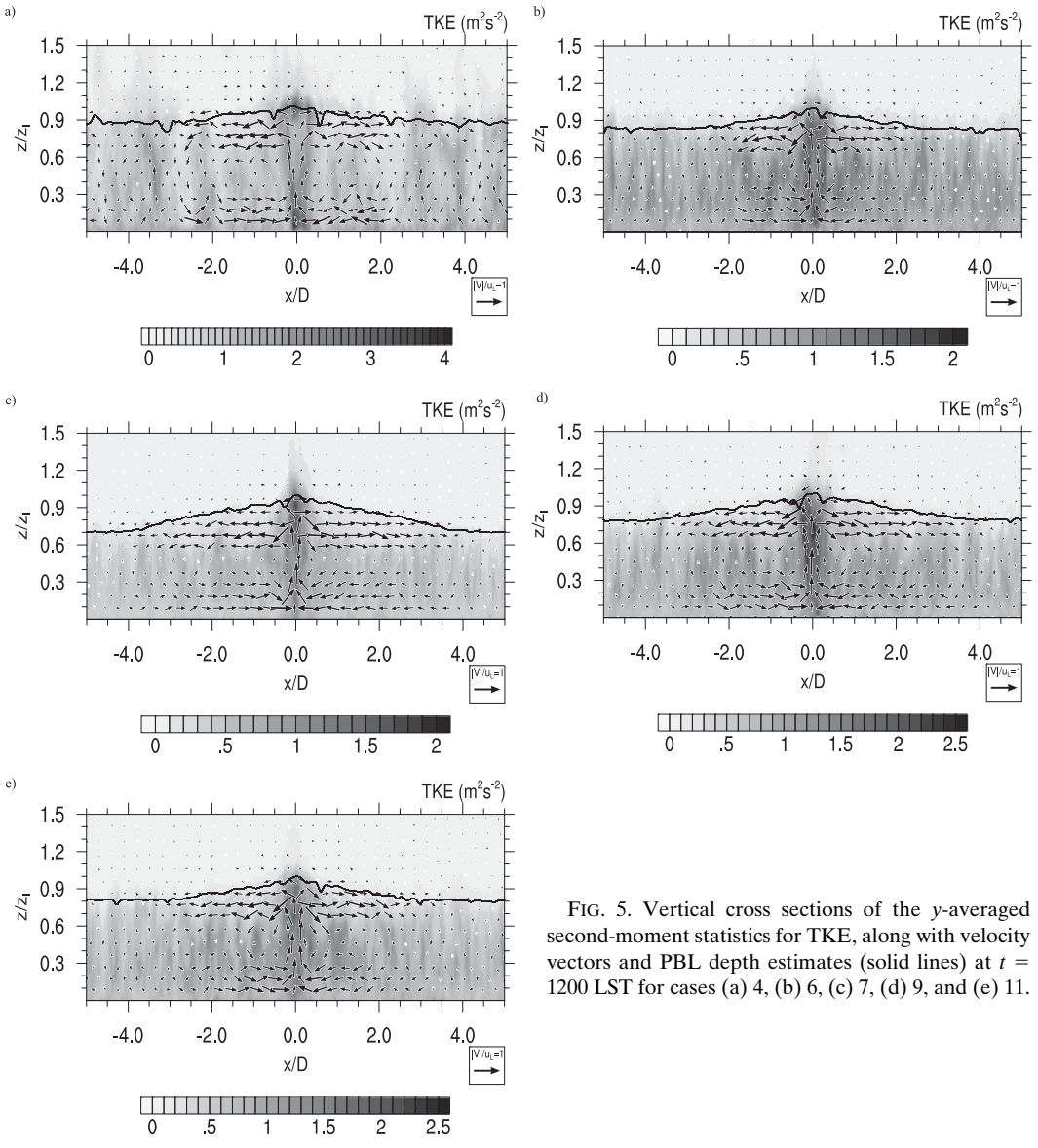

FIG. 5. Vertical cross sections of the y-averaged second-moment statistics for TKE, along with velocity vectors and PBL depth estimates (solid lines) at t = 1200 LST for cases (a) 4, (b) 6, (c) 7, (d) 9, and (e) 11.

which determines lower net radiation at the surface. The TKE presents higher intensity over the entire domain (Fig. 5c); higher values of TKE for cases 7 and 8 are between $0.7 < z/z_i < 1.1$ and an important contribution to the turbulence is given by v and w variances. Variances of horizontal velocity components are slightly influenced by this control parameter, while the w variance displays a maximum larger than in case 1, at $0.8z_i$ (Fig. 8d) The larger value of albedo in case 8 enhances turbulence in a portion of the urban area near the UHI center and determines a maximum of about $1.5\,m^2\,s^{-2}$ at the top of the PBL (not shown). The urban albedo in cases 7 and 8 is the same and then the forcing is the same and thus the scaled heat flux is similar in these cases (Figs. 10a,d).

The effect of reducing urban thermal inertia to values lower than those of the rural area is evident in case 9 (Fig. 5d); the largest values of TKE are located near the UHI center with a light shift of the maximum location from $z/z_i = 0.5$ to $0.6 < z/z_i < 0.7$ and an increase from 2 to $2.5\,m^2\,s^{-2}$. Similarly to cases 7 and 8, the most significant contribution to turbulence in the urban area is given by v and w variance; TKE intensity rapidly decreases from the UHI center toward the rural area.

The anthropogenic heat does not influence the spatial distribution of the TKE, but it tends to increase the TKE

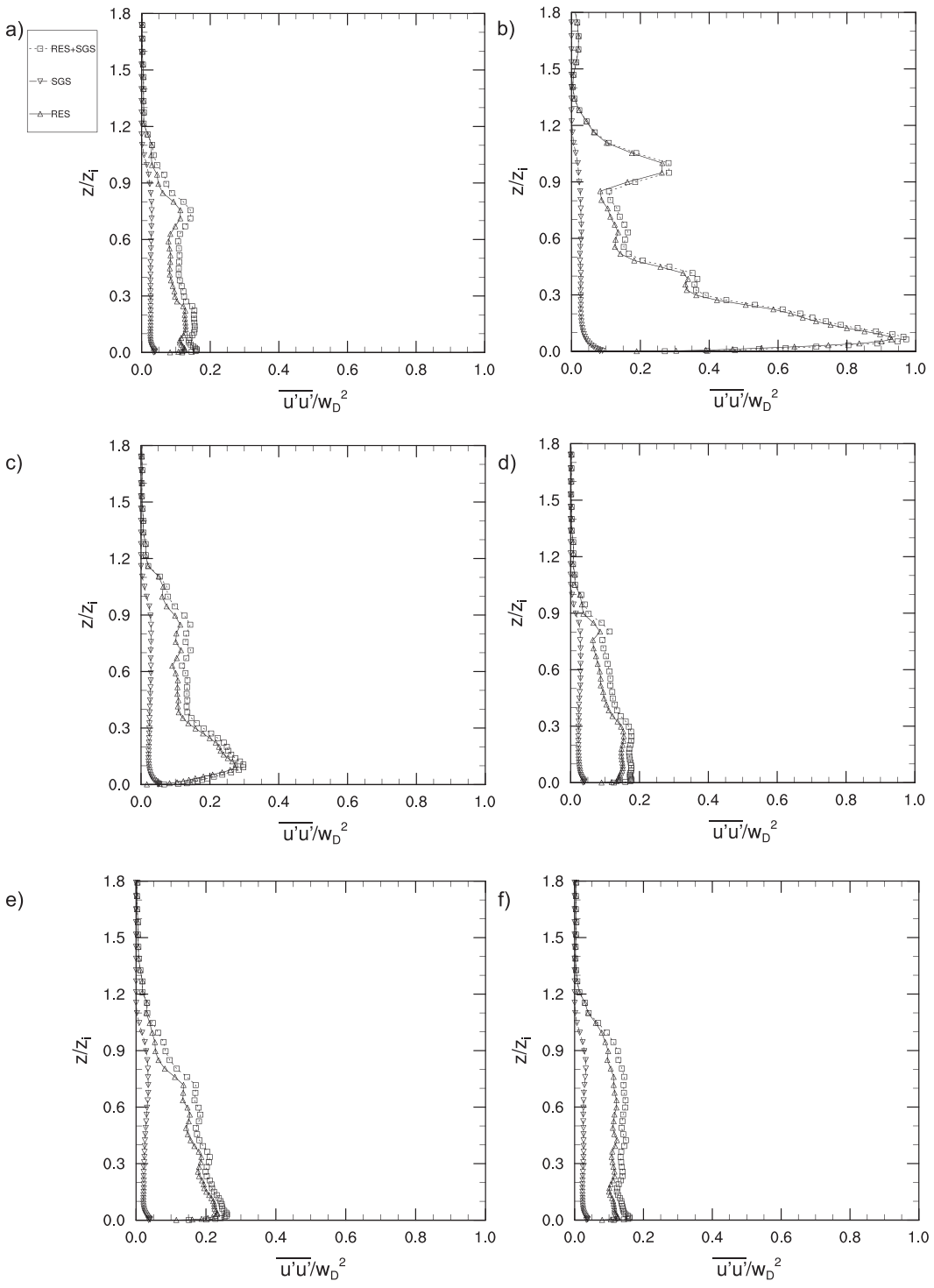

FIG. 6. Vertical profiles of the y-averaged $\overline{u'u'}/w_D^2$ at $x/D = 0$ and $t = 1200$ LST for cases (a) 1, (b) 4, (c) 6, (d) 7, (e) 9, and (f) 11.

values; in particular, the maximum value in case 11 is $2.5\,m^2\,s^{-2}$ (Fig. 5e), while it is $2\,m^2\,s^{-2}$ in case 1 (Fig. 4a). As observed for the albedo contrast, the anthropogenic heat flux influences the value of the scale quantity H_0, and thus the values of the heat flux for case 1 and cases 10 and 11 are similar (Figs. 10a,f).

The vertical profiles of the normalized y-averaged $\overline{u'w'}$ are shown in Fig. 9 for cases 1, 4, 6, 7, 9, and 11 at

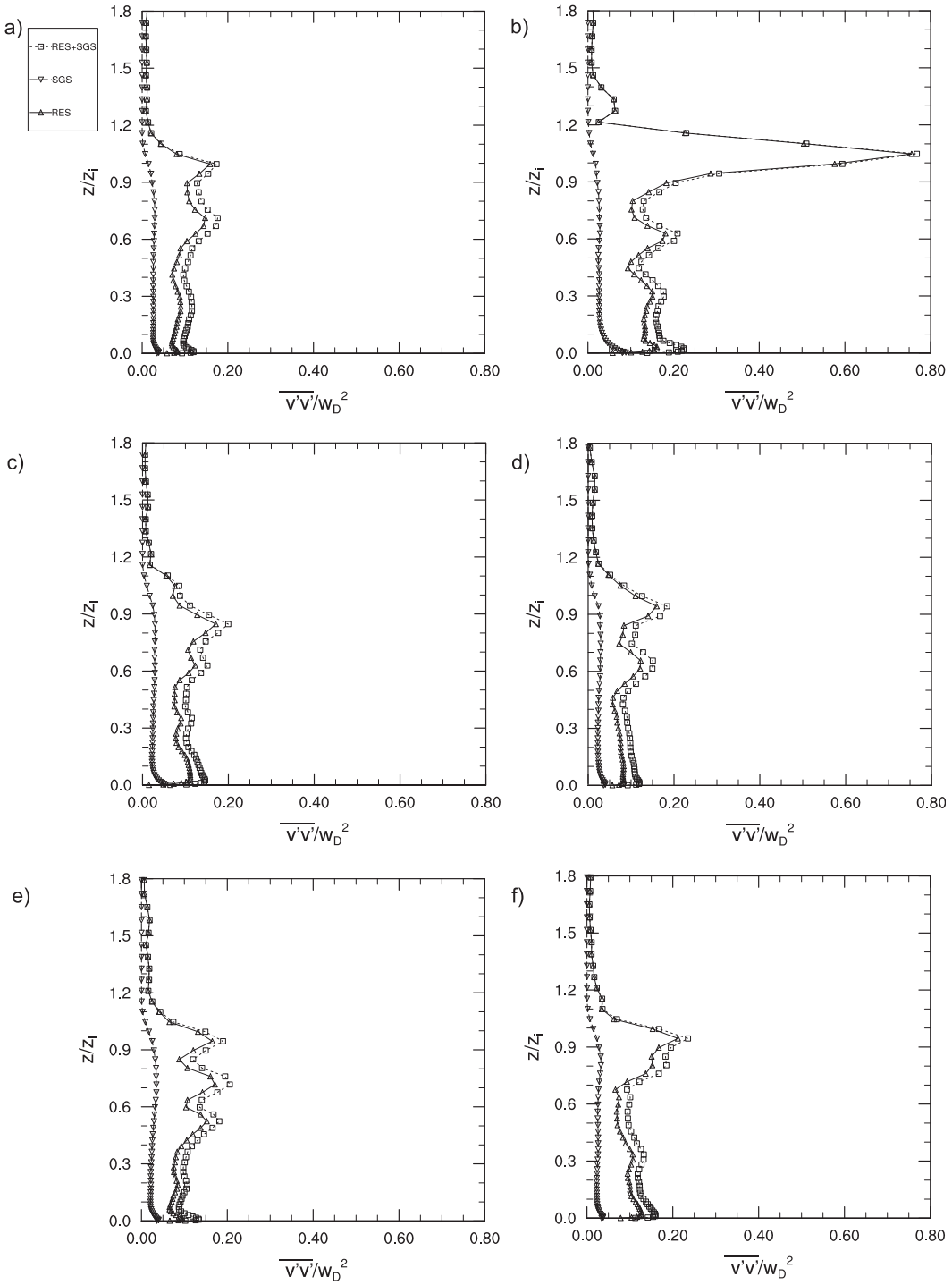

FIG. 7. As in Fig. 6, but for vertical profiles of the y-averaged $\overline{v'v'}/w_D^2$.

$t = 1200$ LST. In case 4, the $\overline{u'w'}$ flux is positive from the surface up to $0.6z_i$ and from $0.9z_i$ to $1.4z_i$; the positive value area extends more than in case 1 and over the PBL top, with values up to 3 times as large as in case 1. The velocity flux is negative between $1.4z_i$ and $1.8z_i$ (Fig. 9b). In case 6, where the control parameter is roughness, the $\overline{u'w'}$ flux is negative in the lower part of the PBL up to $0.9z_i$ and it is positive between $0.9z_i$ and $1.3z_i$ (Fig. 9c). In this case there is a small negative flux area above the PBL depth. Case 7 presents positive

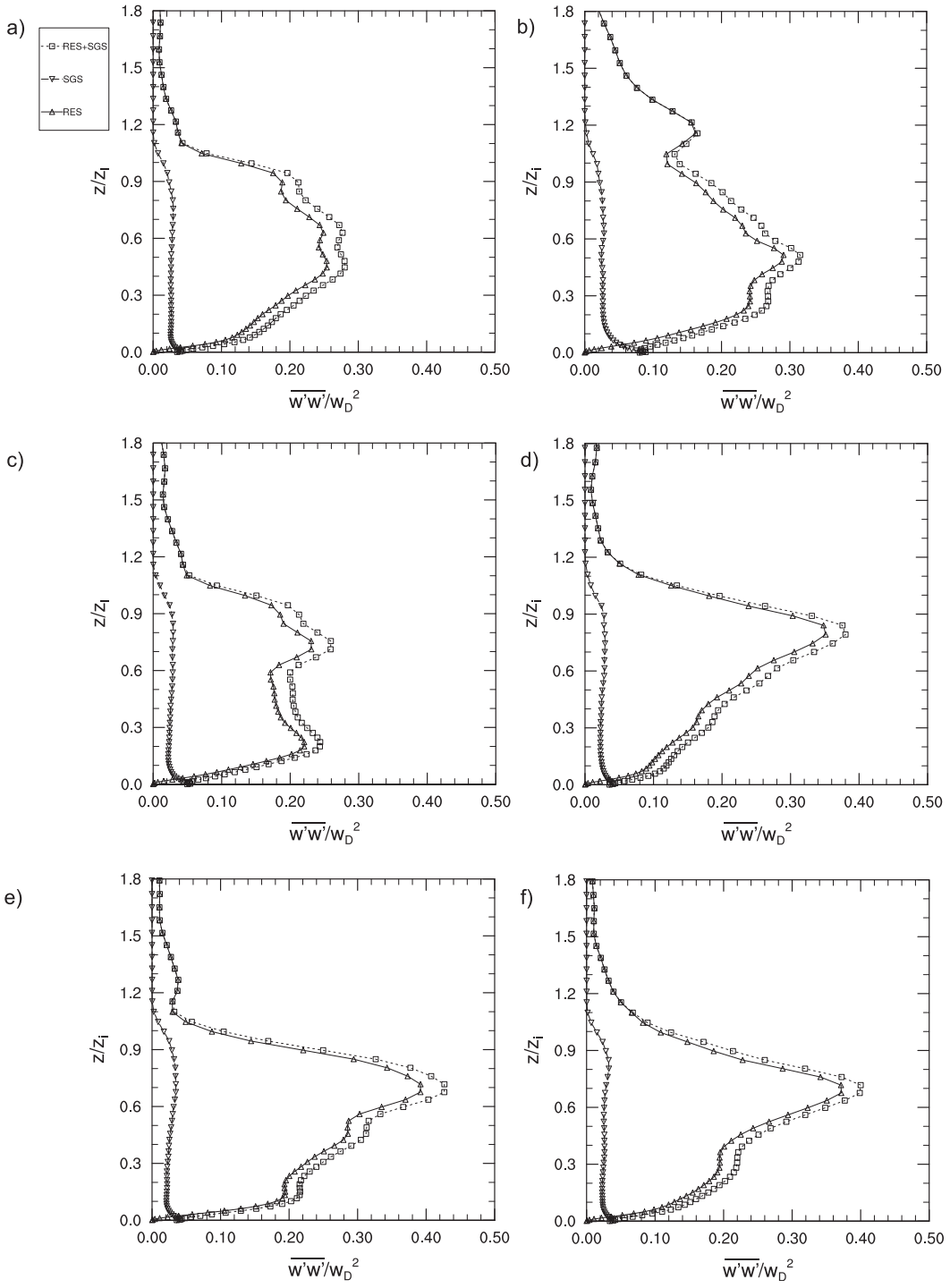

FIG. 8. As in Fig. 6, but for vertical profiles of the y-averaged $\overline{w'w'}/w_D^2$.

$\overline{u'w'}$ values in the lower half of the PBL and negative values in the upper half (Fig. 9d).

Thermal inertia (Fig. 9e) has a large influence on the normalized $\overline{u'w'}$ and the positive values in the lower part of the boundary layer are up to 3 times as large as in case 1. The profile is negative near the surface.

Case 11 (Fig. 9f) shows how the anthropogenic heat flux influences the $\overline{u'w'}$ profile in the lower part of the PBL, where it has negative values up to about $0.3z_i$ and

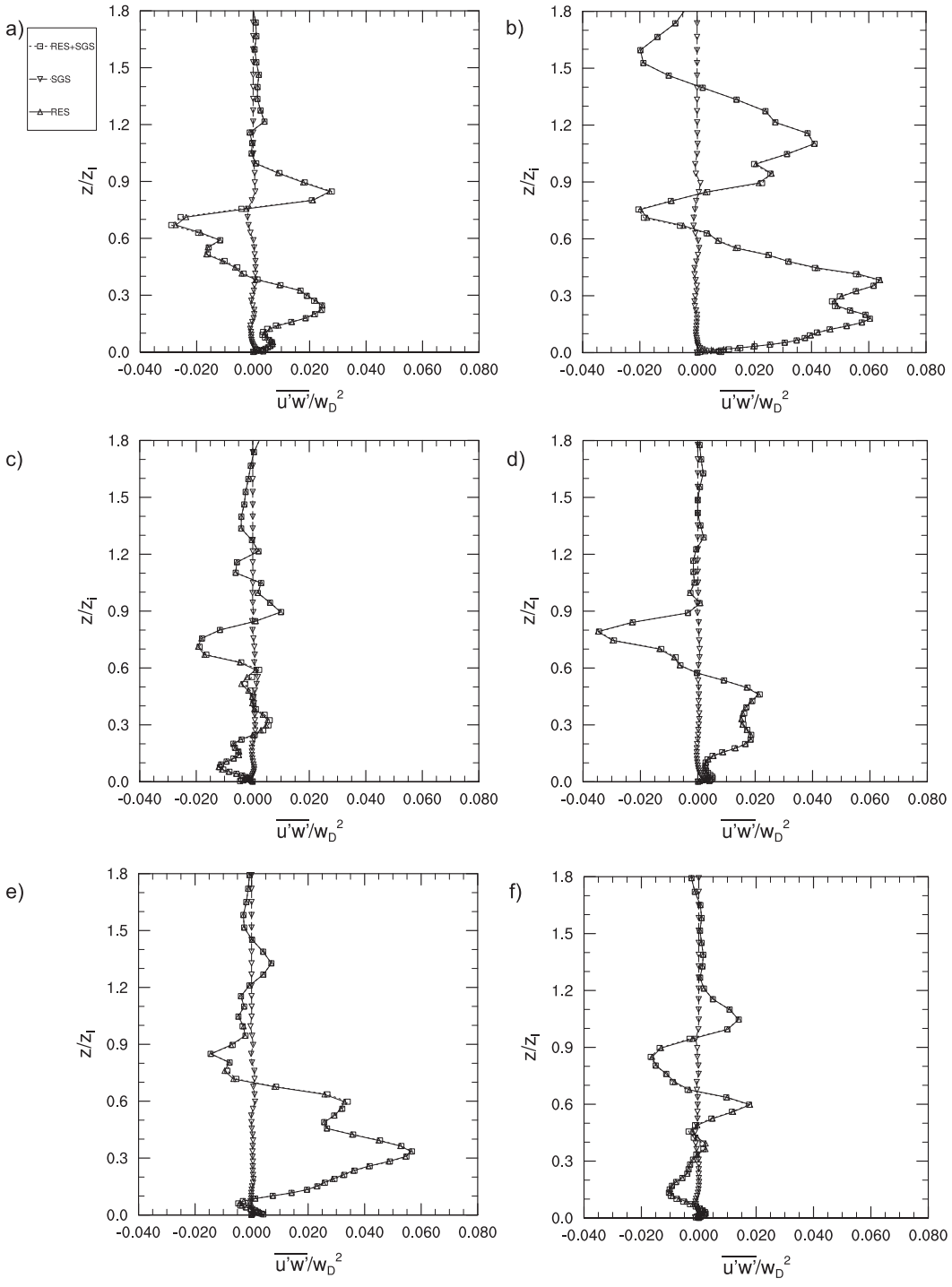

FIG. 9. As in Fig. 6, but for vertical profiles of the y-averaged $\overline{u'w'}/w_D^2$.

positive values from $z = 0.5z_i$ to $0.7z_i$ with a maximum corresponding to $0.6z_i$.

Figures 10a–f show the normalized vertical profiles of the y-averaged heat flux for cases 1, 4, 6, 7, 9, and 11 at $t = 1200$ LST. The presence of the geostrophic wind determines the appearance of a step in the shape of the heat flux between $0.4z_i$ and $0.6z_i$ for cases 2–4. It also influences the negative value, case 4 presenting the lowest value (equal to -0.7). A step in the SHF profile appears also in case 5, while it is

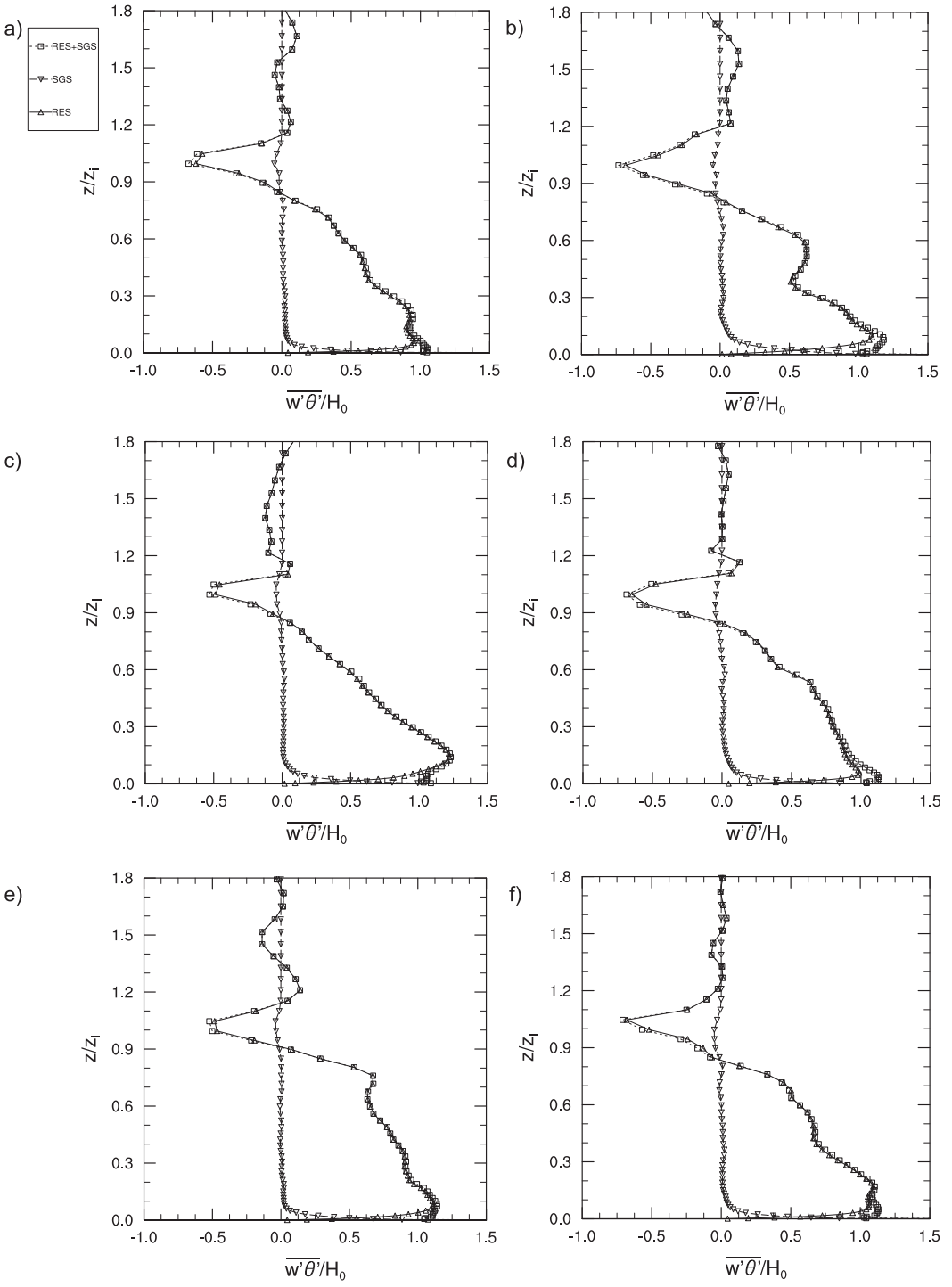

FIG. 10. As in Fig. 6, but for vertical profiles of the y-averaged $\overline{w'\theta'}/H_0$.

not present in case 6 (in both cases the control parameter is roughness). Cases 6, 7, and 9 present a small positive heat flux area above the entrainment region; this area is particularly important in case 9, where it extends from $z = 1.1z_i$ to $1.4z_i$. Cases 6, 7, 9, and 11 show a modest negative flux above the PBL height, which can be related to the presence of gravity waves.

TKE BUDGET ANALYSIS

The budget equation for the total (subgrid plus resolved) TKE reads

$$\frac{\partial E}{\partial t} = -\overline{u}\frac{\partial E}{\partial x} - \overline{w}\frac{\partial E}{\partial z} - \left(\overline{u'^2}\frac{\partial \overline{u}}{\partial x} + \overline{u'w'}\frac{\partial \overline{w}}{\partial x} + \overline{u'v'}\frac{\partial \overline{v}}{\partial x} + \overline{w'^2}\frac{\partial \overline{w}}{\partial z} + \overline{u'w'}\frac{\partial \overline{u}}{\partial z} + \overline{v'w'}\frac{\partial \overline{v}}{\partial z}\right) + \frac{g}{\theta}\overline{w'\theta'} - \left(\frac{\partial}{\partial x}\overline{u'E} + \frac{\partial}{\partial z}\overline{w'E}\right) - \varepsilon, \quad (4)$$

where E is the TKE. The first and second terms on the right-hand side represent the horizontal and vertical advection, respectively (adv_h and adv_v); the third term is the shear production (S); the fourth one is the buoyancy production (B); the fifth one is the turbulent transport (T); and the last term, ε, represents the small-scale dissipation. Partial derivatives in the y direction are removed. The TKE budget is normalized by w_D^3/z_i.

Figure 11a shows the vertical profile of the normalized y-averaged TKE budget at t = 1200 LST for case 1 in correspondence with the UHI center where the highest values of TKE are located, as observed in Fig. 4. The dissipation term is nearly constant with height and balances the buoyancy at the bottom of the domain. The turbulent transport term is the main source of TKE at the PBL top and determines an important redistribution of TKE from the lower half of the PBL to the upper half of the PBL as observed by Moeng and Sullivan (1994) for the convective PBL and Catalano and Moeng (2010) for slope currents. The horizontal advection term is almost equal to zero because of the poor values of both the mean velocity and horizontal gradient; the vertical one has values near zero in the lower part of the PBL and becomes significant in the upper part. The profile of the shear term includes the contribution of both the horizontal and vertical shear; the only significant contributions to this term are given by the u- and w-variance terms. The vertical contribution is negative up to about $z/z_i = 0.5$ (the w variance and the vertical velocity gradient being both positive) and it is positive in the upper part of the layer (the w variance being negative and the vertical velocity gradient being positive); the horizontal shear term is positive in the lower part of the layer (where the flow is convergent), equal to the u-variance profile and negative in the upper part (where the flow is divergent).

The vertical profiles of the y-averaged normalized TKE budget terms for case 1 at t = 1200 LST have been analyzed also in correspondence with the UHI boundary (not shown). There is an evident influence on the buoyancy that decreases linearly up to $z/z_i = 0.4$ and then assumes small negative values, close to zero; it does not have a minimum at the PBL top, typical of a CBL, and its shape is similar to a shear planetary layer (Moeng and Sullivan 1994) because of the strong convergent flow toward the urban area. The horizontal advection, negligible at the UHI center, is more important than the vertical advection up to $z/z_i = 0.3$, as expected; at about $z/z_i = 0.7$ the horizontal and vertical advection terms present the same intensity and opposite sign. In Figs. 11b–f vertical profiles of the TKE budget at the urban area center are shown for cases 4, 6, 7, 9, and 11.

The presence of the geostrophic wind significantly influences the TKE budget terms: the shear contribution reaches its maximum near the surface and for case 4 it is 10 times as large as the maximum of case 1; the term T has a minimum for z between $0.4z_i$ and $0.5z_i$ for case 2 (not shown), while for cases 3 and 4 the profile has a more irregular shape and the intensity of the maximum and the minimum increases; in particular, in case 4, T reaches its maximum at about $z/z_i = 0.1$, which is at the upper limit of the surface layer. Such a high value of the transport term demonstrates that the geostrophic wind has a non-local effect on the TKE. The term B has a small negative value for case 2 (geostrophic wind of $2\,\mathrm{m\,s^{-1}}$) with respect to case 1, and this negative value increases for cases 3 and 4, with a geostrophic wind of 5 and $10\,\mathrm{m\,s^{-1}}$, respectively. The contribution of the horizontal advection is evident near the surface in case 4, where the geostrophic wind has an intensity of $10\,\mathrm{m\,s^{-1}}$. The small-scale dissipation has a minimum of about -2, while it is equal to -0.5 for case 1.

The roughness (Fig. 11c) influences the B profile that has an increase up to about $0.15z_i$ and a maximum between $(0.1–0.2)z_i$; it influences also the T profile especially in the lower part in case 6 and in the upper part of case 5 (not shown).

Figure 11d (case 7) shows that the change of the urban–rural albedo gap has a negligible effect on B, while it influences S and one of the two maxima, of about 0.3 in case 1, disappears; in cases 7 and 8 S has a maximum larger than in case 1 at about $z/z_i = 0.8$, equal to 0.6 in case 7 and to 0.5 in case 8 (not shown). The term T contributes significantly to the redistribution of the TKE with a minimum of 0.5 at about $z/z_i = 0.6$ and a maximum of 1 at $0.9z_i$.

The effect of the thermal inertia on TKE budget terms is evident in case 9 (Fig. 11e). The dissipation term rapidly decreases from the surface to near-zero values and displays an anomalous bulge up to the PBL top; the shear term presents one maximum in the upper part of the layer with an intensity 3 times larger than in case 1. The vertical advection term presents a minimum and a maximum 2 times larger (as absolute value) than in case 1.

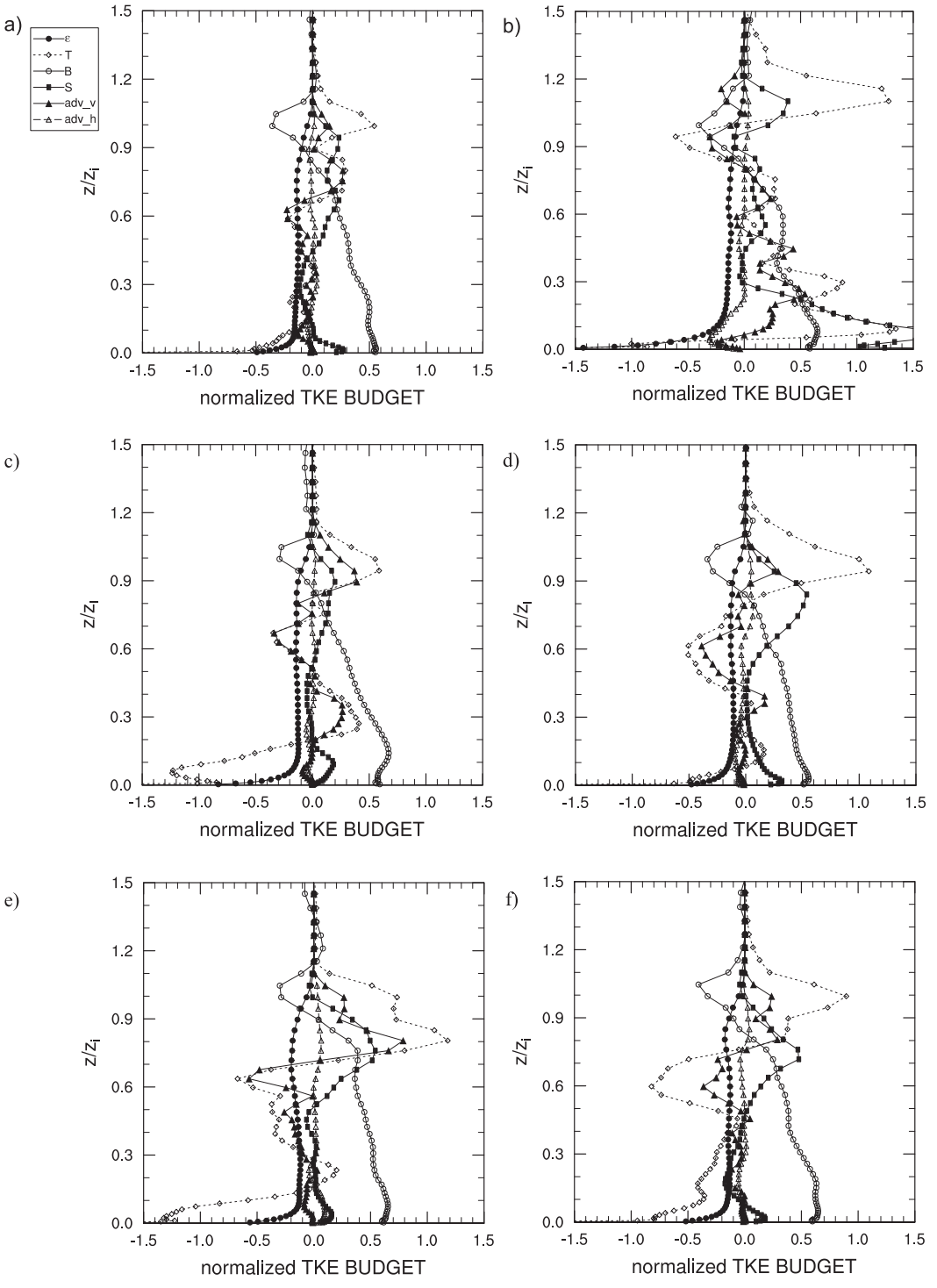

FIG. 11. Similar to Fig. 6, but for normalized vertical profiles of the *y*-averaged TKE budget.

The values of anthropogenic heat influence the intensity of T, S, and the vertical advection terms. In cases 10 and 11, the normalized shear has a maximum in the upper part of the boundary layer of about 0.5, exactly at $0.7z_i$ and at $0.8z_i$, respectively. The transport term is significant in cases 10 and 11 up to $0.2z_i$ and $0.4z_i$. The negative value of T at $0.6z_i$ is present also in cases 10 and 11, but it is more important; similarly, the maximum

value in correspondence with the PBL top is 2 times as large as in case 1.

4. Conclusions

The high-resolution study of an idealized diurnal UHI circulation was carried out using the WRF Model in LES mode. To reproduce the surface inhomogeneities driving the UHI phenomenon, the code was modified to differentiate the surface properties of the urban surface from those of the rural area.

For the first time, the effect of relevant control parameters on the PBL structure in terms of variances, fluxes, and TKE budget was investigated. Control parameters considered for the simulations are surface roughness length, albedo, thermal inertia, and anthropogenic heat flux. The effect of geostrophic wind intensity on the UHI circulation and turbulence characteristics has been also analyzed. Albedo, thermal inertia, and anthropogenic heat appear in the SEB equation and directly influence the UHI intensity. The roughness does not appear in the SEB equation but influences the UHI intensity because of its inhibiting effect on the thermal growth. The geostrophic wind of intensity equal to 2, 5, and 10 $\mathrm{m\,s^{-1}}$ has a light influence on the UHI intensity.

The presence of the UHI determines horizontal heterogeneities in the PBL for both kinematic and thermal variables; a significant impact on the mixing-layer height is given by the urban–rural albedo gap.

The geostrophic wind plays a crucial role in the variances, especially of horizontal velocity components, and therefore on the TKE intensity, both over urban and rural areas.

The investigation of the TKE budget shows that the geostrophic wind influences the TKE intensity and its spatial distribution and determines a considerable redistribution of the TKE budget, while albedo and anthropogenic heat flux have a great impact on the TKE magnitude. The higher albedo difference between urban and rural areas determines lower absolute values of the TKE budget normalized profiles. Thermal inertia values influence the dissipation profile, which presents a bulge up to the PBL top, and the maximum value of the vertical advection term.

The results of the present study confirm that the bulk properties of the UHI phenomenon depend on the ratio between z_i/D and Fr. It has been found that the plot (z_i/D) versus Fr, created by comparing literature data and numerical results obtained by this study, clearly connects the plume height over the city to the bottom thermal forcing (through the SHF), to the ambient stability (through the Brunt–Väisälä frequency), and to the horizontal extension of the urban area.

Such results can help to evaluate the role of land-cover changes and the associated alterations of radiative, thermal, and aerodynamic properties on local properties of the PBL. They can also be used to provide scenarios to evaluate the expected effects of the strategies for the mitigation of the UHI phenomenon (e.g., building materials with higher albedo, insulating materials for walls).

This kind of investigation, based on nondimensional parameters and characteristic dimensions, shows the importance of a proper scaling theory. The development of a new scale theory, considering also surface properties (e.g., albedo or thermal inertia), is a very interesting topic for a future work.

Furthermore, the analysis of higher-order statistics (variances, fluxes, and TKE budget) distribution at the high spatial resolution of 50 m represents an innovative contribution to knowledge of the UHI phenomenon and, more generally, of phenomena characterized by a spatial inhomogeneity. This analysis may provide useful parameters for pollution dispersion models; such insights can be applied also in the wind energy engineering field.

The numerical modeling tool used in this work and based on the WRF Model has proved to be a valid tool that makes it possible to simulate the UHI circulation, taking into account the ambient geostrophic wind and the surface properties. Nevertheless, before its use for realistic simulations, improvements are required, for example, the inclusion of the moisture in the atmosphere, of the Bowen ratio term in the SEB, of a realistic orography, and of the effects of the urban canyons. Furthermore, with the inclusion of the hydrological cycle, this model could represent a tool for the investigation of the UHI effects (e.g., land use, surface and air temperature, wind intensity, or heat flux) on natural hazards.

Acknowledgments. This study was funded by the Italian Ministry of Education, University and Research and by the Department of Civil, Constructional and Environmental Engineering (DICEA) of Sapienza University of Rome. Simulations were performed on the in-house computing facilities of DICEA. The authors thank Antonio Cenedese and Branko Kosovic for their helpful discussions.

REFERENCES

Akbari, H., M. Pomerantz, and H. Taha, 2001: Cool surfaces and shade trees to reduce energy use and improve air quality in urban areas. *Sol. Energy*, **70**, 295–310, doi:10.1016/S0038-092X(00)00089-X.

Bryan, G. H., and J. M. Fritsch, 2002: A benchmark simulation for moist nonhydrostatic numerical models. *Mon. Wea.*

Rev., **130**, 2917–2928, doi:10.1175/1520-0493(2002)130<2917:ABSFMN>2.0.CO;2.

Burridge, D. M., and A. J. Gadd, 1975: The Meteorological Office operational 10-level numerical weather prediction model. British Meteorological Office Tech. Notes 12 and 48, 57 pp.

Catalano, F., and A. Cenedese, 2010: High-resolution numerical modeling of thermally driven slope winds in a valley with strong capping. *J. Appl. Meteor. Climatol.*, **49**, 1859–1880, doi:10.1175/2010JAMC2385.1.

——, and C.-H. Moeng, 2010: Large-eddy simulation of the daytime boundary layer in an idealized valley using the weather research and forecasting numerical model. *Bound.-Layer Meteor.*, **137**, 49–75, doi:10.1007/s10546-010-9518-8.

——, A. Cenedese, S. Falasca, and M. Moroni, 2011: High resolution numerical and experimental modeling of the urban heat island circulation. *Proc. VII Int. Symp. on Stratified Flows*, Rome, Italy, Sapienza University of Rome. [Available from F. Catalano, ENEA, Casaccia, Via Anguillarese, 301, 00123 Santa Maria di Galeria - Roma, Italy.]

——, ——, ——, and ——, 2012a: Numerical and experimental simulations of local winds. *National Security and Human Health Implications of Climate Change*, H. Fernando, Z. Klaić, and J. L. McCulley, Eds., Springer, 199–218.

——, M. Moroni, V. Dore, and A. Cenedese, 2012b: An alternative scaling for unsteady penetrative free convection. *J. Geophys. Res.*, **117**, D18102, doi:10.1029/2012JD018229.

Cenedese, A., and P. Monti, 2003: Interaction between an inland urban heat island and a sea-breeze flow: A laboratory study. *J. Appl. Meteor.*, **42**, 1569–1583, doi:10.1175/1520-0450(2003)042<1569:IBAIUH>2.0.CO;2.

Chen, X.-L., H.-M. Zhao, P.-X. Li, and Z.-Y. Yin, 2006: Remote sensing image-based analysis of the relationship between urban heat island and land use/cover changes. *Remote Sens. Environ.*, **104**, 133–146, doi:10.1016/j.rse.2005.11.016.

Clarke, J. F., and J. L. McElroy, 1974: Effects of ambient meteorology and urban morphological features on the vertical temperature structure over cities. Preprint, *Air Pollution Control Association 67th Annual Meeting*, Denver, CO, Air Pollution Control Association, Paper 74-73. [Available from J. F. Clarke, MD-80, U.S. Environmental Protection Agency, Research Triangle Park, NC 27711.]

Deardorff, J. W., 1978: Efficient prediction of ground surface temperature and moisture, with inclusion of a layer of vegetation. *J. Geophys. Res.*, **83**, 1889–1903, doi:10.1029/JC083iC04p01889.

Dudhia, J., 1989: Numerical study of convection observed during the winter monsoon experiment using a mesoscale two-dimensional model. *J. Atmos. Sci.*, **46**, 3077–3107, doi:10.1175/1520-0469(1989)046<3077:NSOCOD>2.0.CO;2.

European Environment Agency, 2014: Global megatrend 2: Towards a more urban world. Assessment of global megatrends—An update, European Environment Agency Rep., 20 pp. [Available online at http://www.eea.europa.eu/publications/global-megatrends-update-2/at_download/file.]

Falasca, S., M. Moroni, and A. Cenedese, 2013: Laboratory simulations of an urban heat island in a stratified atmospheric boundary layer. *J. Visualization*, **16**, 39–45, doi:10.1007/s12650-012-0150-1.

Faust, K. M., 1981: Modelldarstellung von Wärmeinselströmungen durch konvektionsstrahlen. Ph.D. dissertation, Universität Karlsruhe, 144 pp.

Filho, E. P. M., M. Cassol, H. A. Caram, and U. Rizza, 2013: The vertical structure of tropical urban heat island with LES. *Amer. J. Environ. Eng.*, **3**, 24–31, doi:10.5923/j.ajee.20130301.05.

Giovannini, L., D. Zardi, and M. de Franceschi, 2011: Analysis of the urban thermal fingerprint of the city of Trento in the Alps. *J. Appl. Meteor. Climatol.*, **50**, 1145–1165, doi:10.1175/2010JAMC2613.1.

——, ——, ——, and F. Chen, 2014: Numerical simulations of boundary-layer processes and urban-induced alterations in an Alpine valley. *Int. J. Climatol.*, **34**, 1111–1131, doi:10.1002/joc.3750.

Godowitch, J. M., J. K. S. Ching, and J. F. Clarke, 1987: Spatial variation of the evolution and structure of the urban boundary layer. *Bound.-Layer Meteor.*, **38**, 249–272, doi:10.1007/BF00122447.

Grimmond, C. S. B., and T. R. Oke, 1999: Heat storage in urban areas: Local-scale observations and evaluation of a simple model. *J. Appl. Meteor.*, **38**, 922–940, doi:10.1175/1520-0450(1999)038<0922:HSIUAL>2.0.CO;2.

Hidalgo, J., G. Pigeon, and V. Masson, 2008: Urban-breeze circulation during the CAPITOUL experiment: Observational data analysis approach. *Meteor. Atmos. Phys.*, **102**, 223–241, doi:10.1007/s00703-008-0329-0.

——, V. Masson, and L. Gimeno, 2010: Scaling the daytime urban heat island and urban-breeze circulation. *J. Appl. Meteor. Climatol.*, **49**, 889–901, doi:10.1175/2009JAMC2195.1.

Hinkel, K. M., F. E. Nelson, A. E. Klene, and J. H. Bell, 2003: The urban heat island in winter at Barrow, Alaska. *Int. J. Climatol.*, **23**, 1889–1905, doi:10.1002/joc.971.

Kim, Y.-H., and J.-J. Baik, 2002: Maximum urban heat island intensity in Seoul. *J. Appl. Meteor.*, **41**, 651–659, doi:10.1175/1520-0450(2002)041<0651:MUHIII>2.0.CO;2.

Kristof, G., N. Rácz, and M. Balogh, 2009: Adaptation of pressure based CFD solvers for mesoscale atmospheric problems. *Bound.-Layer Meteor.*, **131**, 85–103, doi:10.1007/s10546-008-9325-7.

Kurbatskii, A. F., 2001: Computational modeling of the turbulent penetrative convection above the urban heat island in a stably stratified environment. *J. Appl. Meteor.*, **40**, 1748–1761, doi:10.1175/1520-0450(2001)040<1748:CMOTTP>2.0.CO;2.

Kusaka, H., and F. Kimura, 2004: Coupling a single-layer urban canopy model with a simple atmospheric model: Impact on urban heat island simulation for an idealized case. *J. Meteor. Soc. Japan*, **82**, 67–80, doi:10.2151/jmsj.82.67.

Lee, S.-H., and J.-J. Baik, 2010: Statistical and dynamical characteristics of the urban heat island intensity in Seoul. *Theor. Appl. Climatol.*, **100**, 227–237, doi:10.1007/s00704-009-0247-1.

Li, D., and E. Bou Zeid, 2013: Synergistic interaction between urban heat island and heat waves: The impact in cities is larger than the sum of its parts. *J. Appl. Meteor. Climatol.*, **52**, 2051–2064, doi:10.1175/JAMC-D-13-02.1.

——, ——, M. L. Baek, S. Jessup, and J. A. Smith, 2013: Modeling land surface processes and heavy rainfall in urban environments: Sensitivity to urban surface representations. *J. Hydrometeor.*, **14**, 1098–1118, doi:10.1175/JHM-D-12-0154.1.

Lu, J., S. P. Arya, W. H. Snyder, and R. E. Lawson Jr., 1997a: A laboratory study of the urban heat island in a calm and stably stratified environment. Part I: Temperature field. *J. Appl. Meteor.*, **36**, 1377–1391, doi:10.1175/1520-0450(1997)036<1377:ALSOTU>2.0.CO;2.

——, ——, ——, and ——, 1997b: A laboratory study of the urban heat island in a calm and stably stratified environment. Part II: Velocity field. *J. Appl. Meteor.*, **36**, 1392–1402, doi:10.1175/1520-0450(1997)036<1392:ALSOTU>2.0.CO;2.

Martilli, A., 2002: Numerical study of urban impact on boundary layer structure: Sensitivity to wind speed, urban morphology, and rural soil moisture. *J. Appl. Meteor.*, **41**, 1247–1266, doi:10.1175/1520-0450(2002)041<1247:NSOUIO>2.0.CO;2.

Miao, S., F. Chen, Q. Li, and S. Fan, 2011: Impacts of urban processes and urbanization on summer precipitation: A case study of heavy rainfall in Beijing on 1 August 2006. *J. Appl. Meteor. Climatol.*, **50**, 806–825, doi:10.1175/2010JAMC2513.1.

Milojevic, A., P. Wilkinson, B. Armstrong, M. Davis, A. Mavrogianni, S. Bohnenstengel, and S. Belcher, 2011: Impact of London's urban heat island on heat-related mortality. *Epidemiology*, **22**, 182–183, doi:10.1097/01.ede.0000392239.91165.65.

Moeng, C.-H., and P. P. Sullivan, 1994: A comparison of shear- and buoyancy- driven planetary boundary layer flows. *J. Atmos. Sci.*, **51**, 999–1022, doi:10.1175/1520-0469(1994)051<0999:ACOSAB>2.0.CO;2.

Monin, A. S., and A. M. Obukhov, 1954: Basic laws of turbulent mixing in the surface layer of the atmosphere. *Tr. Akad. Nauk SSSR Geophiz. Inst.*, **24**, 163–187.

Richiardone, R., and G. Brusasca, 1989: Numerical experiments on urban heat island intensity. *Quart. J. Roy. Meteor. Soc.*, **115**, 983–995, doi:10.1002/qj.49711548811.

Roth, M., 2000: Review of atmospheric turbulence over cities. *Quart. J. Roy. Meteor. Soc.*, **126**, 941–990, doi:10.1002/qj.49712656409.

Ryu, Y.-H., J.-J. Baik, and J.-Y. Han, 2013: Daytime urban breeze circulation and its interaction with convective cells. *Quart. J. Roy. Meteor. Soc.*, **139**, 401–413, doi:10.1002/qj.1973.

Salamanca, F., A. Martilli, M. Tewari, and F. Chen, 2011: A study of the urban boundary layer using different urban parameterizations and high-resolution urban canopy parameters with WRF. *J. Appl. Meteor. Climatol.*, **50**, 1107–1128, doi:10.1175/2010JAMC2538.1.

Skamarock, W. C., and Coauthors, 2008: A description of the Advanced Research WRF version 3. NCAR Tech. Note NCAR/TN-475+STR, 113 pp., doi:10.5065/D68S4MVH.

Snyder, W. H., 1981: Guideline for fluid modeling of atmospheric diffusion. EPA Rep. EPA-600/8-81-009, 200 pp. [Available online at http://nepis.epa.gov/Adobe/PDF/2000BDW8.PDF.]

Sullivan, P. P., C.-H. Moeng, B. Stevens, D. Lenschow, and S. D. Mayor, 1998: Structure of the entrainment zone capping the convective atmospheric boundary layer. *J. Atmos. Sci.*, **55**, 3042–3064, doi:10.1175/1520-0469(1998)055<3042:SOTEZC>2.0.CO;2.

Wang, W., 2009: The influence of thermally-induced mesoscale circulations on turbulence statistics over an idealized urban area under a zero background wind. *Bound.-Layer Meteor.*, **131**, 403–423, doi:10.1007/s10546-009-9378-2.

Yoshikado, H., 1992: Numerical study of the daytime urban effect and its interaction with the sea breeze. *J. Appl. Meteor.*, **31**, 1146–1164, doi:10.1175/1520-0450(1992)031<1146:NSOTDU>2.0.CO;2.